Interpretative 3D MHD modelling of deuterium shattered pellet injection into a JET H-mode plasma

M. Kong[1], E. Nardon[2], M. Hoelzl[3], D. Bonfiglio[4], D. Hu[5], U. Sheikh[6], A. Boboc[1], P. Carvalho[1], T.C. Hender[1], S. Jachmich[7], K.D. Lawson[1], S. Silburn[1], Ž. Štancar[1], R. Sweeney[8], G. Szepesi[1], the JOREK team* and JET contributors†

[1] *UKAEA-CCFE, Culham Science Centre, Abingdon, Oxon, OX14 3DB, UK*

[2] *CEA, IRFM, F-13108 Saint-Paul-lez-Durance, France*

[3] *Max Planck Institute for Plasma Physics, Boltzmannstr. 2, 85748 Garching b. M., Germany*

[4] *Consorzio RFX, Corso Stati Uniti 4, 35127 Padova, Italy*

[5] *School of Physics, Beihang University, Beijing, 100191, China*

[6] *École Polytechnique Fédérale de Lausanne (EPFL), Swiss Plasma Center (SPC), CH-1015 Lausanne, Switzerland*

[7] *ITER Organization, Route de Vinon sur Verdon, CS 90 046, 13067 Saint Paul-lez-Durance, Cedex, France*

[8] *Massachusetts Institute of Technology, Cambridge, MA 02139, USA*

Introduction

Shattered pellet injection (SPI) is the current solution for the ITER disruption mitigation system (DMS) to prevent disruption-related damage. Compared with impurity SPI, deuterium (D_2) SPI could contribute to runaway electron (RE) avoidance via strong dilution cooling before thermal quench (TQ) [1,2]. However, the drifts of ablation plasmoids towards the tokamak low field side (LFS) [3,4] and the existence of background impurities [2] could put this strategy into question. In this work, we have performed detailed modelling of a JET D_2 SPI discharge with JOREK [5], focusing on these two aspects. The JET H-mode plasma considered (#96874) has a plasma current $I_p \approx 3\,\mathrm{MA}$, thermal energy $W_{\mathrm{th}} \approx 7\,\mathrm{MJ}$, central electron temperature $T_{\mathrm{e0}} \approx 7\,\mathrm{keV}$ and central electron density $n_{\mathrm{e0}} \approx 8.5 \times 10^{19}\mathrm{m}^{-3}$ before the SPI [6,7]. A D_2 pellet with about 1.6×10^{23} atoms was launched and broke into two pieces before shattering, leading to two groups of shards arriving at the plasma about 3.5 ms apart (25% atoms contained in the 1st group). The pre-TQ duration, defined here as the time elapsed from the time when the 1st group of shards reach the plasma edge ($t = 0$ in this paper) to the I_p spike, is about 9.5 ms.

Numerical model and simulation setup

The basic model used consists of reduced MHD equations, diffusive neutrals and an extension for SPI [1]. The ablation rate is estimated by $N' \propto r_s^{1.33} n_e^{0.33} T_e^{1.64}$, where r_s is the shard radius, n_e the electron density and T_e the electron temperature. The ablated neutrals are deposited around each shard with a Gaussian shape in the toroidal, poloidal and minor radius directions, the half e^{-1} width of which are set to 0.5 rad, 15 cm and 2 cm in this paper. Radiative cooling rates of

*See the author list of M. Hoelzl et al Nucl. Fusion 61 065001 (2021)

†See the author list of J. Mailloux et al Nucl. Fusion 62 042026 (2022)

background impurities are estimated using ADAS data and assuming coronal equilibrium. We are limited by spatial resolution of 3D simulations to directly resolve ablation plasmoid drifts. Instead, we propose a "teleportation" model to account for the particle and energy transfers resulting from drifts. The general idea is as follows: shifting the ablation neutral source along the outward R direction by a certain distance (Δ_{drift}) from the shard's location; transferring energy from the shard location to the deposited neutral location. The energy transfer rate corresponds to the ablation neutral source times a few tens of electron volts (ΔE) to consider the overall effects of dissociation, ionization, radiation and early heating before plasmoid drifts.

The JOREK grid used comprises about 22000 finite elements on the poloidal plane and up to $n = 10$ Fourier components toroidally. $T_i = T_e$ is assumed. Spitzer resistivity η_{sp} is kept for T_e up to 1.7 keV, above which the resistivity is uniform. Central resistivity $\eta_0 \approx 5\eta_{sp}$. Spitzer-Härm parallel heat diffusivity is used, while perpendicular heat diffusivity $\kappa_\perp \approx 2\,\mathrm{m}^2/\mathrm{s}$. Parallel particle transport is purely convective except at the entry of post-drift plasmoids for numerical reasons, while $D_\perp \approx 2\,\mathrm{m}^2/\mathrm{s}$. The bulk velocity of the two groups of shards is 300 and 260 m/s, respectively, and each with a $\pm 40\%$ velocity spread. The shard radii are distributed according to a fragmentation model [8], with 280 and 32 shards in the two groups, respectively. Only small shards are present in the front and rear of the shard plume based on lab measurements [9].

Effects of ablation plasmoid drifts on SPI shard ablation and penetration

Drifts of high-β plasmoids formed by the ablated material of frozen pellets have been observed in hydrogen isotope pellet fuelling experiments, e.g., plasmoids have shown to traverse 20% of the minor radius in about 10 μs in AUG experiments [10]. In JET #96874, evident outward motion of shards was observed by the fast camera, possibly due to a rocket effect associated with plasmoid drifts [10]. In fact, as shown by the red curve in Fig. 1 (a), the JOREK simulation without plasmoid drifts clearly overestimates the central line-integrated density.

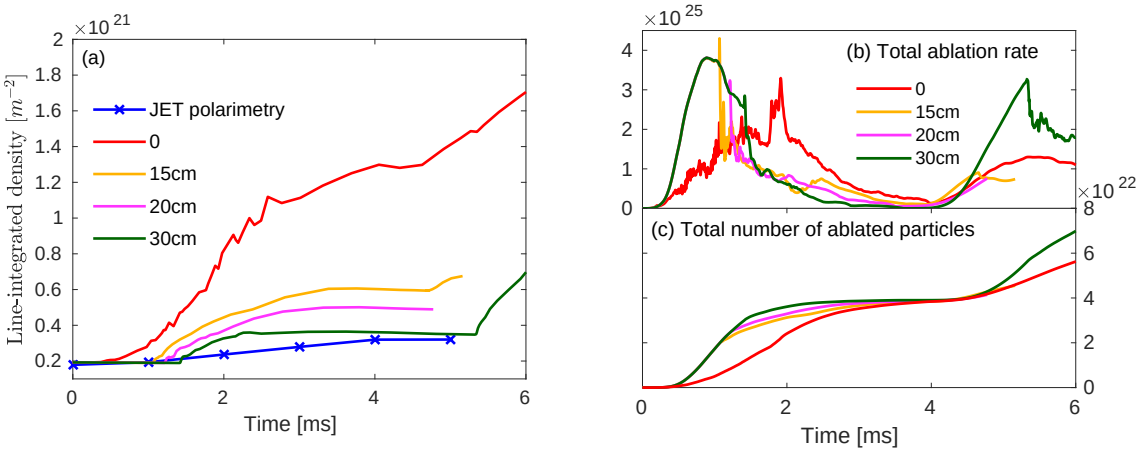

Figure 1: Scan of drift distance with $1 \times 10^{17}\mathrm{m}^{-3}$ background neon and $4.5 \times 10^{15}\mathrm{m}^{-3}$ tungsten.

The effects of drifts are studied with the proposed teleportation model and fixed $\Delta E = 50\,\mathrm{eV}$: scans within its theoretical range do not show much difference. As for Δ_{drift}, a scaling law exists for fuelling hydrogen pellets [11], but may not be directly applied to SPI cases considering the modification of plasma profiles and interactions among plasmoids that were not included in the scaling law. Given the uncertainties, we have assumed the same Δ_{drift} for all ablation plasmoids at this stage. Simulations with $\Delta_{\mathrm{drift}} = 15, 20$ and $30\,\mathrm{cm}$ are depicted in Fig. 1. $30\,\mathrm{cm}$ matches best the measured density evolution. The total ablation rate N' of all the shards, as shown in Fig. 1 (b), is much higher for the cases with drifts (before the entry of the post-drift ablation plasmoids indicated by the spikes). This is due to lower dilution cooling and higher local T_e with drifts. After the arrival of post-drift plasmoids, N' drops sharply and remains lower than in the case without drifts due to smaller shard radii remaining. The 1st group of shards are fully ablated at $t \approx 4\,\mathrm{ms}$, as observed by the fast camera. Simulations suggest a shallower penetration when considering plasmoid drifts given the strong ablation, as illustrated in Fig. 2.

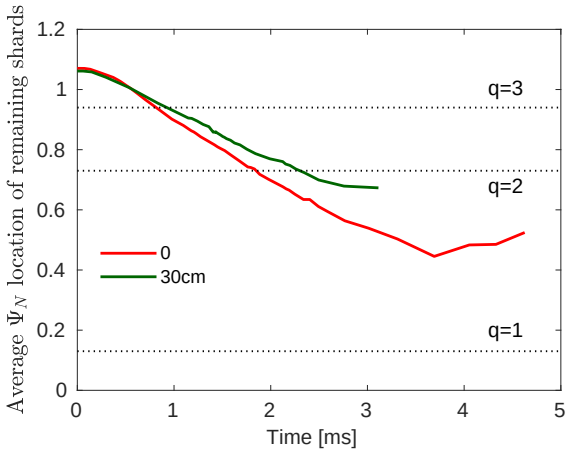

Figure 2: Average normalized Ψ location of the remaining shards from the 1st group at each time slice for the red and green cases shown in Fig. 1.

Effects of background impurities on radiative cooling during D_2 SPI

Background impurities could dominate radiative cooling during D_2 SPI due to their ability to radiate more strongly [2]. In JET #96874, neon and carbon densities are $n_{\mathrm{NE}} \approx n_{\mathrm{C}} \approx 1 \times 10^{17}\mathrm{m}^{-3}$ based on charge exchange measurements before the SPI; tungsten density $n_{\mathrm{W}} \approx 4.5 \times 10^{15}\mathrm{m}^{-3}$ is predicted with the 1.5D transport code JINTRAC, neglecting other (high charge number) impurities that were present. We have performed scans of n_{NE} and n_{C} assuming spatially uniform distributions and fixed $\Delta_{\mathrm{drift}} = 30\,\mathrm{cm}$ (that matches the measured density). As shown in Fig. 3 (a), background neon plays a key role in the radiative cooling during SPI, especially in the sharp P_{rad} increase at $t \approx 6\,\mathrm{ms}$. This can be explained by the T_e-dependence of the radiative cooling rates of different species, among which the radiative cooling rate of neon increases by two orders of magnitude from 150 to $30\,\mathrm{eV}$. As shown in Fig. 4, neon radiation peaks at $T_e = 30\,\mathrm{eV}$. We also note the effect of plasmoid drifts on P_{rad} in Fig. 3 (a): the sharp increase of P_{rad} is missing for the case without drifts (red curve). This could be explained by the higher ablation rate during the 2nd group of shards for cases with $\Delta_{\mathrm{drift}} = 30\,\mathrm{cm}$ (green versus red traces in Fig. 1 (b)), which could lead to higher local pressure gradient and stronger MHD

activity. As shown in Fig. 3 (b), high-n modes are excited and eventually lead to a fast growth of all harmonics. These high-n modes are probably resistive interchange modes enabled by edge cooling (Fig. 4), similar to those evoked in relation to the Greenwald limit [12].

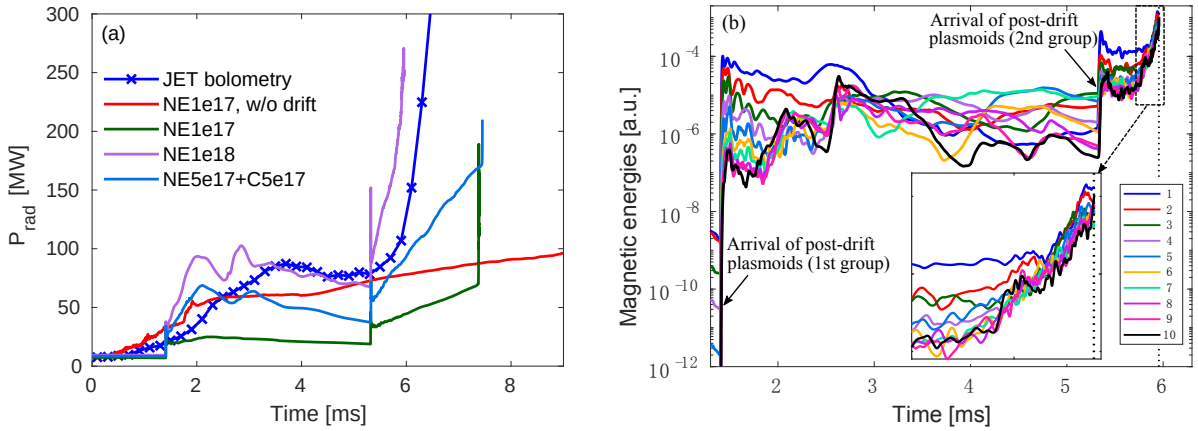

Figure 3: (a) Scan of n_{NE} and n_{C} with $\Delta_{\mathrm{drift}} = 30\,\mathrm{cm}$ (except for the red curve) and $n_{\mathrm{W}} = 4.5 \times 10^{15}\mathrm{m}^{-3}$. (b) Magnetic energy evolution of the purple case in Fig. 3 (a).

Conclusions and outlook

The pre-TQ dynamics of a JET D_2 SPI discharge have been studied in detail with JOREK. With a new teleporation model, ablation plasmoid drifts are shown to limit the penetration of LFS D_2 SPI and affect MHD activity. Background impurities, especially neon in the considered JET discharge, are shown to dominate radiative cooling during D_2 SPI by comparing with measurements. These could affect the effectiveness of D_2 SPI in RE avoidance and need to be considered in ITER predictions. In future studies, we will explore the effects of non-uniform drift distance and finite mixture of neon in the pellet on plasmoid drifts. Further validation of D_2 SPI against additional experiments on JET and AUG are also envisaged.

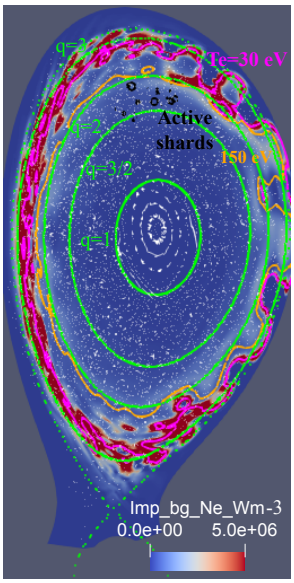

Figure 4: Neon radiation for the purple case in Fig. 3 (a) at $t \approx 6\,\mathrm{ms}$.

This work has been carried out within the framework of the EUROfusion Consortium, funded by the European Union via the Euratom Research and Training Programme (Grant Agreement No 101052200 — EUROfusion) and from the EPSRC [grant number EP/T012250/1]. To obtain further information on the data and models underlying this paper please contact PublicationsManager@ukaea.uk. Views and opinions expressed are however those of the author(s) only and do not necessarily reflect those of the European Union or the European Commission or the ITER organization. Neither the European Union nor the European Commission can be held responsible for them.

References

[1] D. Hu et al, Nucl. Fusion **58**, 126025 (2018)
[2] E. Nardon et al, Nucl. Fusion **60**, 126025 (2020)
[3] B. Pégourié, Plasma Phys. Control. Fusion **49**, R87 (2007)
[4] A. Matsuyama, Phys. Plasmas **29**, 042501 (2022)
[5] M. Hoelzl et al, Nucl. Fusion **61**, 065001 (2021)
[6] S. Jachmich et al, Nucl. Fusion **62**, 026012 (2022)
[7] U.A. Sheikh et al, Nucl. Fusion **61**, 126043 (2021)
[8] T.E. Gebhart et al, IEEE Trans. Plasma Sci. **48**, 1598 (2020)
[9] T.E. Gebhart et al, Fusion Sci. Tech. **77**, 33 (2021)
[10] H.W. Müller, et al, Nucl. Fusion **42**, 301 (2002)
[11] F. Köchl et al, 35th EPS Conference, P4.099 (2008)
[12] M. Giacomin et al, Phys. Rev. Lett. **128**, 185003 (2022)